Supporting Information

Synchronously reconfiguring closed pore and interlayer spacing of wood-derived hard carbon via hot-pressing for advanced sodium-ion batteries

Yangyang Chen, Yu Liao, Yiding Ding, Ying Wu, Lei Li, Sha Luo, Yan Qing, Zhihan Li, Zhen Zhang, and Yiqiang Wu**

College of Materials Science and Technology, Central South University of Forestry and Technology, Changsha 410004, China.

*Corresponding author

E-mail: qingyan0429@163.com

1. Experimental section

1.1 Characterization

The microstructure of the prepared materials was observed using a scanning electron microscope (SEM, HITACHI S-4800) and a transmission electron microscope (TEM, JEOL, JEM-2100). The crystal structure and defect characteristics of the prepared materials were characterized using an X-ray diffractometer (XRD, Rigaku, Ultima IV) and a Raman spectrometer (Jobin Yvon, Labram-010). The chemical composition of the prepared materials was analyzed using X-ray photoelectron spectroscopy (XPS, ESCALAB250), Fourier transform infrared spectroscopy (FTIR, BRUKER TENSOR II), and thermogravimetric analysis (TGA, STA6000). The specific surface area and pore structure of the prepared materials were tested using a surface area analyzer (Micromeritics, ASAP 2020 HD). The closed-pore structure of the prepared materials was analyzed using small-angle X-ray scattering (SAXS, Anton Paar Saxsess MC2). By measuring the true density of the test material, the pore volume of the material can be analyzed (Micromeritics, AccuPyc II 1340).

1.2 Electrochemical measurements

The coin cells (CR 2016) were assembled in a Mikrouna glove box under high-purity argon protection, with water and oxygen contents both below 1 ppm. The prepared hard carbon material, polyvinylidene fluoride (PVDF) binder, and acetylene black conductive agent were thoroughly ground and mixed in a mass ratio of 8:1:1. A suitable amount of N-methyl-2-pyrrolidone (NMP) solvent was added, and the mixture was stirred for 10 hours to obtain a uniform slurry. This slurry was evenly coated onto a copper foil using a scraper and dried in a vacuum drying oven at 80 °C for 12 hours. The dried electrode sheets were then punched into 12 mm diameter disks, with a loading mass of over 1.5 mg. Glass fiber was used as the separator, self-made sodium foil as both the counter and reference electrodes, and 1 M $NaPF_6$ dissolved in DME was used as the electrolyte. The cells were tested for cycling performance and rate capability using a CT3002A battery testing system. The voltage range for cell testing was set from 0.005 V to 3 V, and the current density range was from 0.1 to 4 A g^{-1}. The cells underwent cyclic voltammetry testing using an electrochemical workstation (CHI 660), with a voltage window from 0.005 V to 3 V and a scan rate range of 0.2 to 1 mV s^{-1}. The diffusion coefficient of Na^+ in the material was obtained through Galvanostatic Intermittent Titration Technique (GITT) tests using the CT3002A system. These tests employed a pulse current of 50 μA for 0.5 hours with a relaxation time of 1 hour.

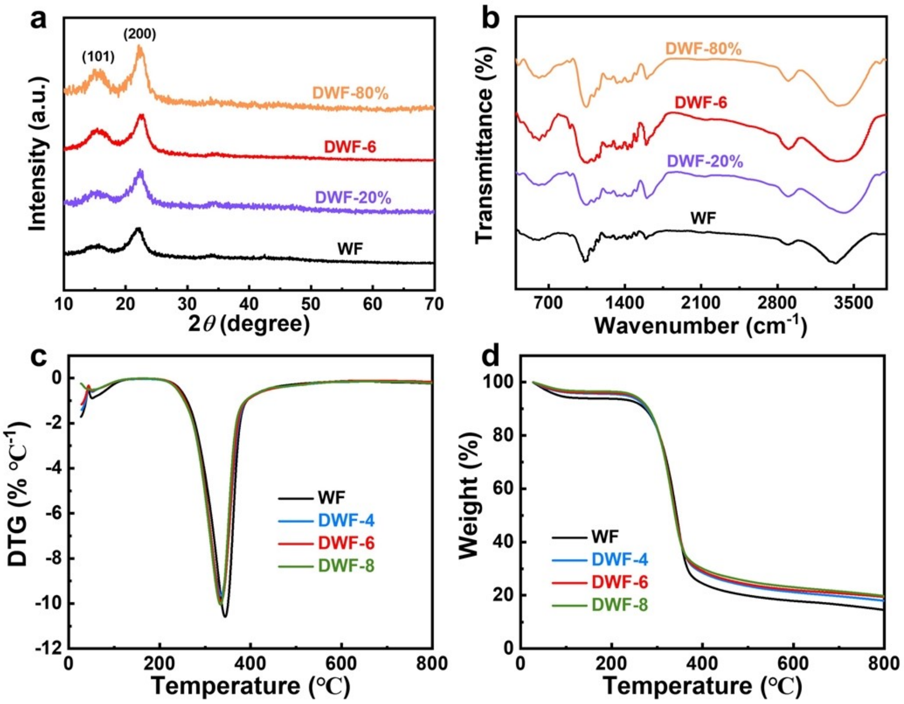

Fig. S1 XRD patterns (a) and Raman spectra (b) of WF and DWF–*x*, respectively. The thermogravimetric differential curves (c) of WF and DWF–*P*. The TGA curves (d) of WF and DWF–*P*.

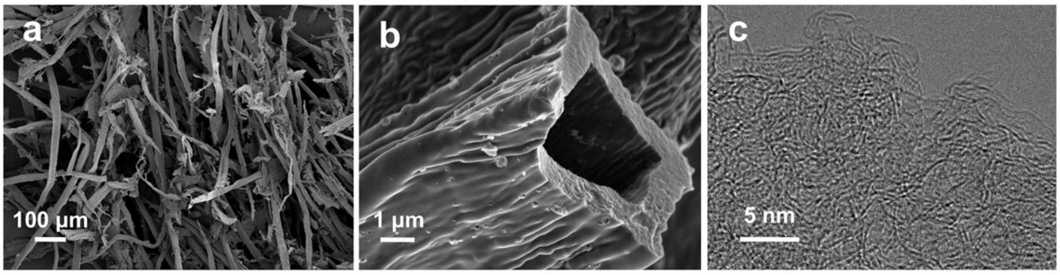

Fig. S2 SEM images of WF (a) and CWF (b). HRTEM image of CWF.

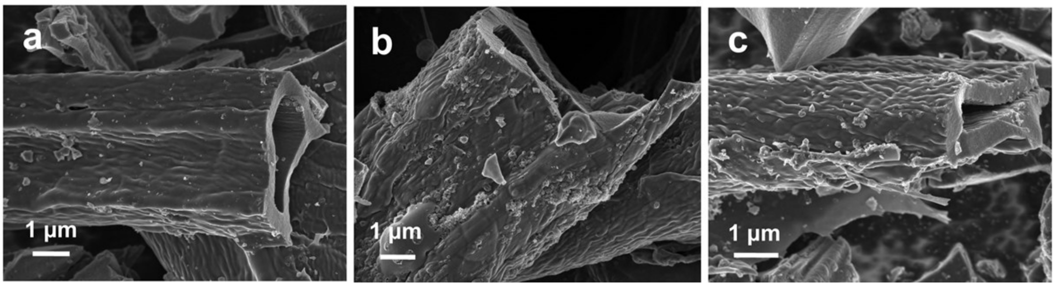

Fig. S3 SEM images of DWF–4 (a), DWF–6 (b), and DWF–8 (c).

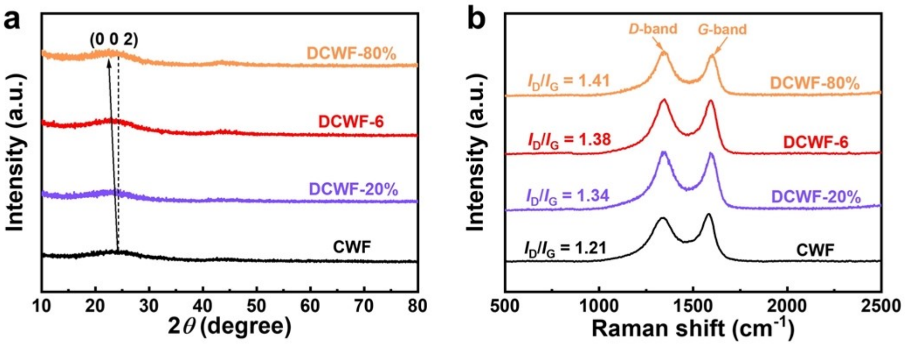

Fig. S4 XRD patterns (a) and Raman spectra (b) of CWF and DCWF–*x*, respectively.

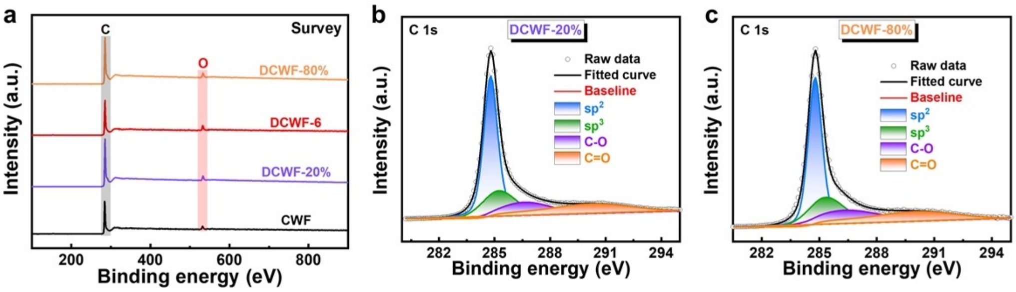

Fig. S5 XPS spectra (a) of CWF and DCWF–*x*. C 1s XPS high-resolution spectra of DCWF–20% (b) and DCWF–80% (c), respectively.

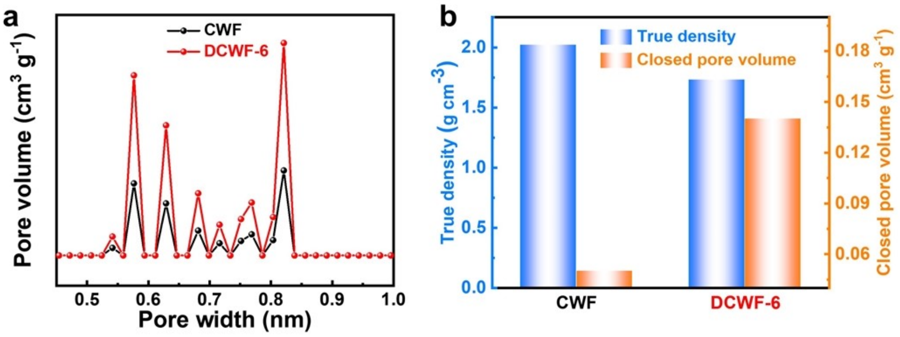

Fig. S6 Pore size distribution of CWF and DCWF–6 under CO_2 atmosphere (a). True density and closed pore volume of CWF and DCWF−6 (b).

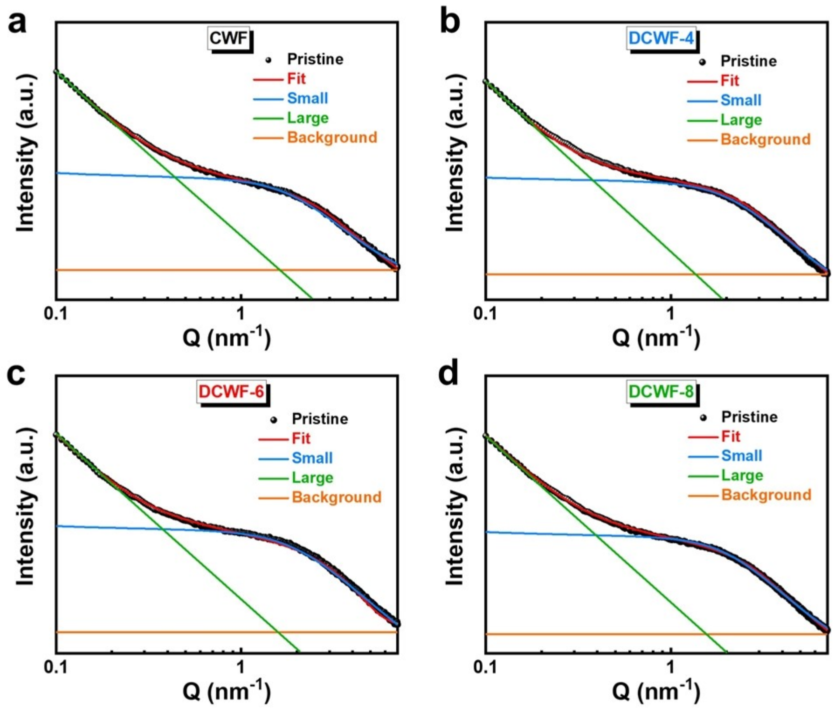

Fig. S7 Fitted SAXSs patterns of CWF (a), DCWF–4 (b), DCWF–6 (c) and DCWF–8 (d), respectively.

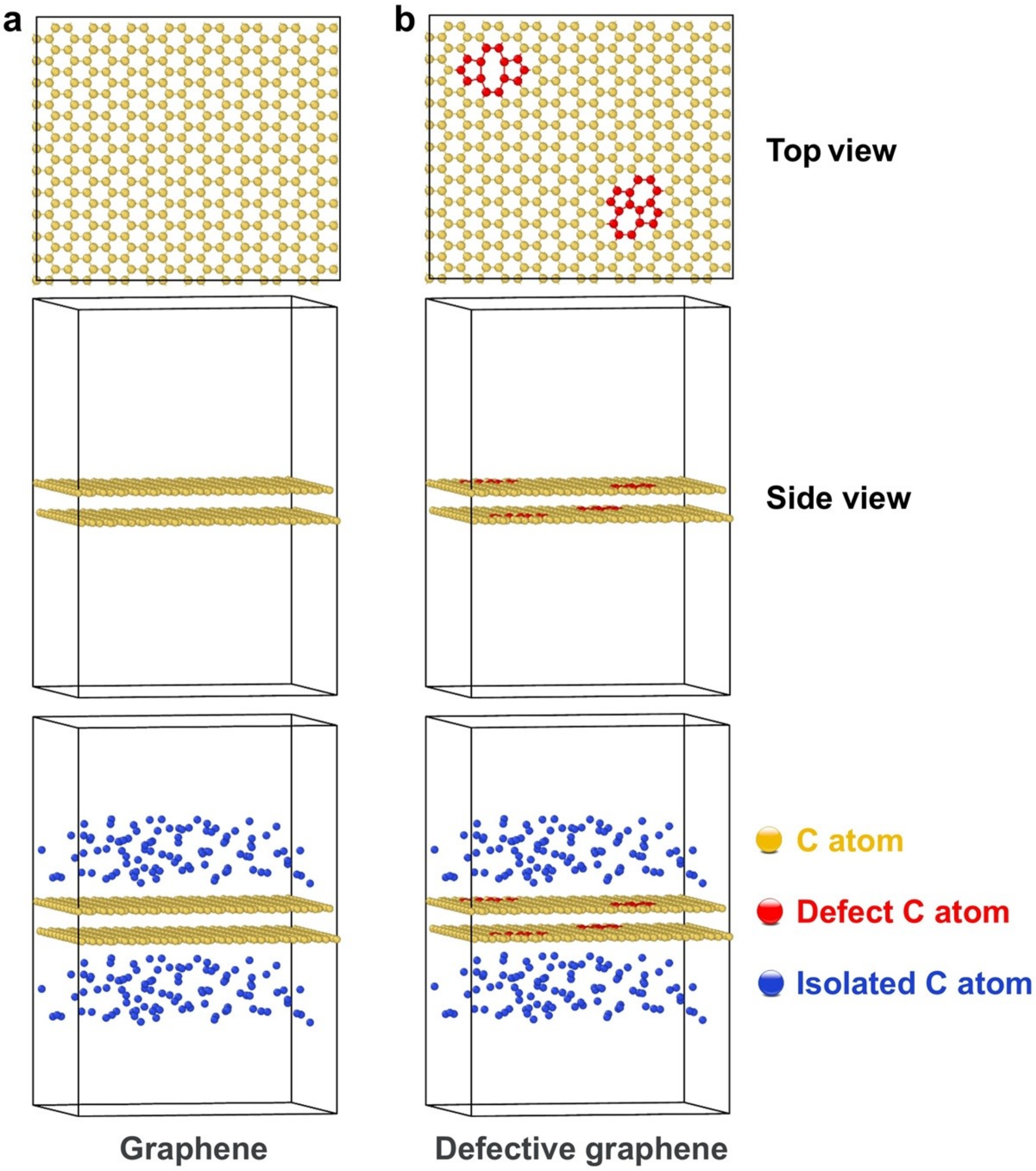

Fig. S8 Graphene structure (a). Top view, side view, graphene structure with isolated C atoms. Graphene structure with defects (b). Top view, side view, graphene structure with defects and isolated C atoms.

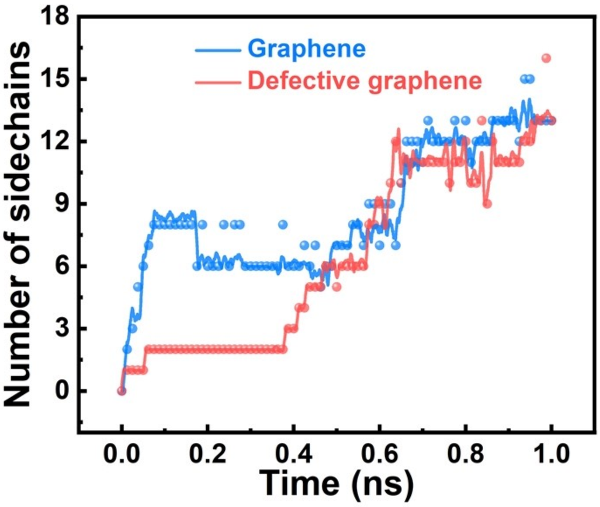

Fig. S9 The number of bonds between isolated carbon atoms and graphene.

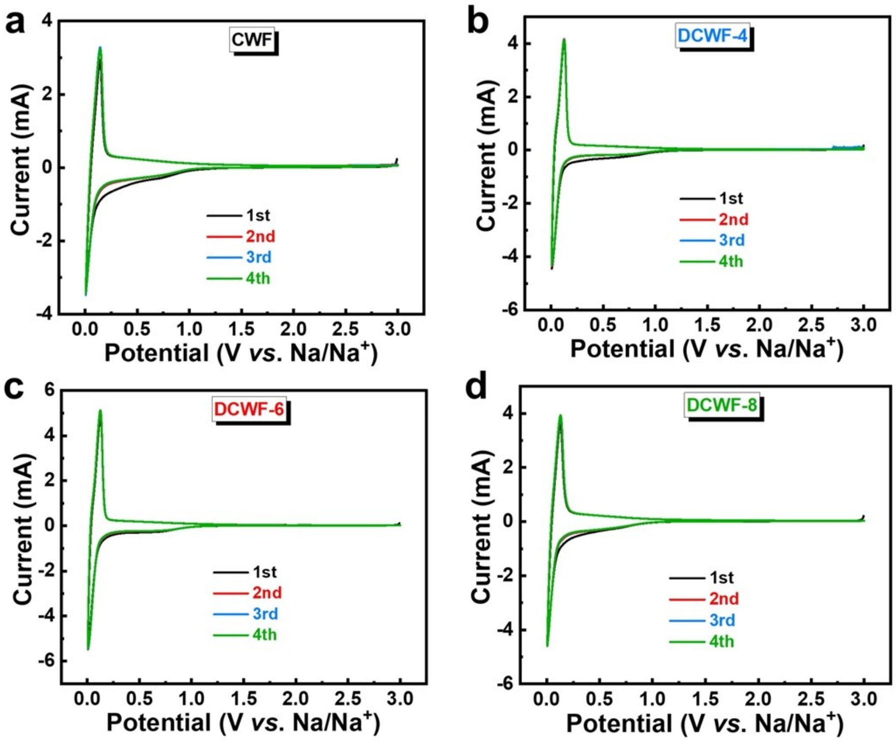

Fig. S10 Cyclic voltammetry profiles of the first four cycles for CWF (a), DCWF–4 (b), DCWF–6 (c) and DCWF–8 (d) electrodes, respectively.

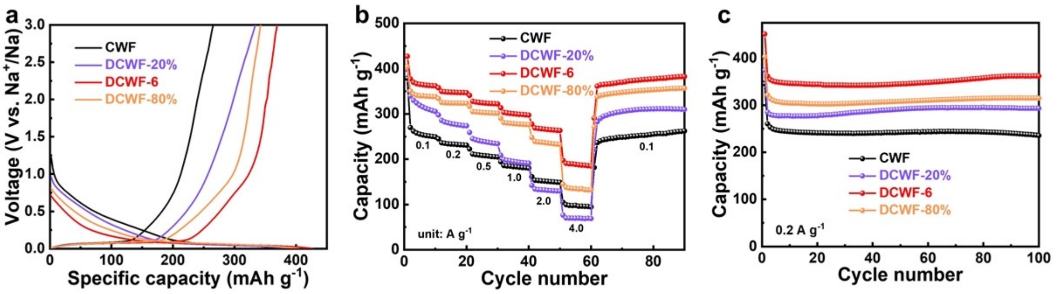

Fig. S11 The first discharge–charge curves (a) of CWF and DCWF–*x* at the current density of 0.1 A g^{-1}. Rate performance (b) of CWF and DCWF–*x*. Cycling performance (c) of CWF and DCWF–*x* at the current density of 0.2 A g^{-1}.

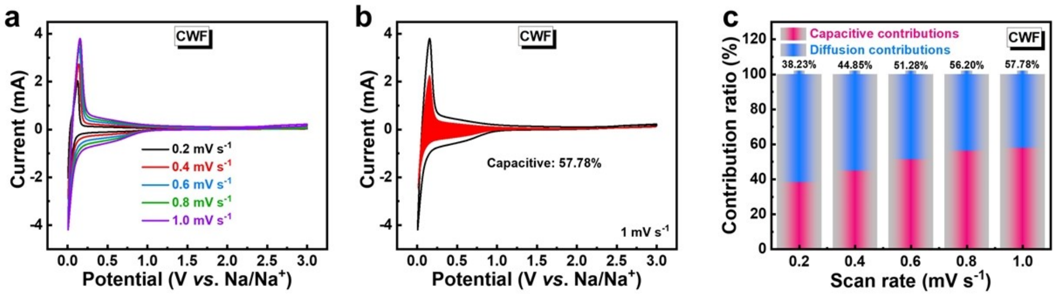

Fig. S12 Cyclic voltammetry curves of CWF electrode with scan rates from 0.2 to 1.0 mV s^{-1} (a). The distribution of capacitive behaviors of CWF measured at 1 mV s^{-1} (b). The contribution ratio of the capacitive capacity of CWF electrode at various scan rates (c).

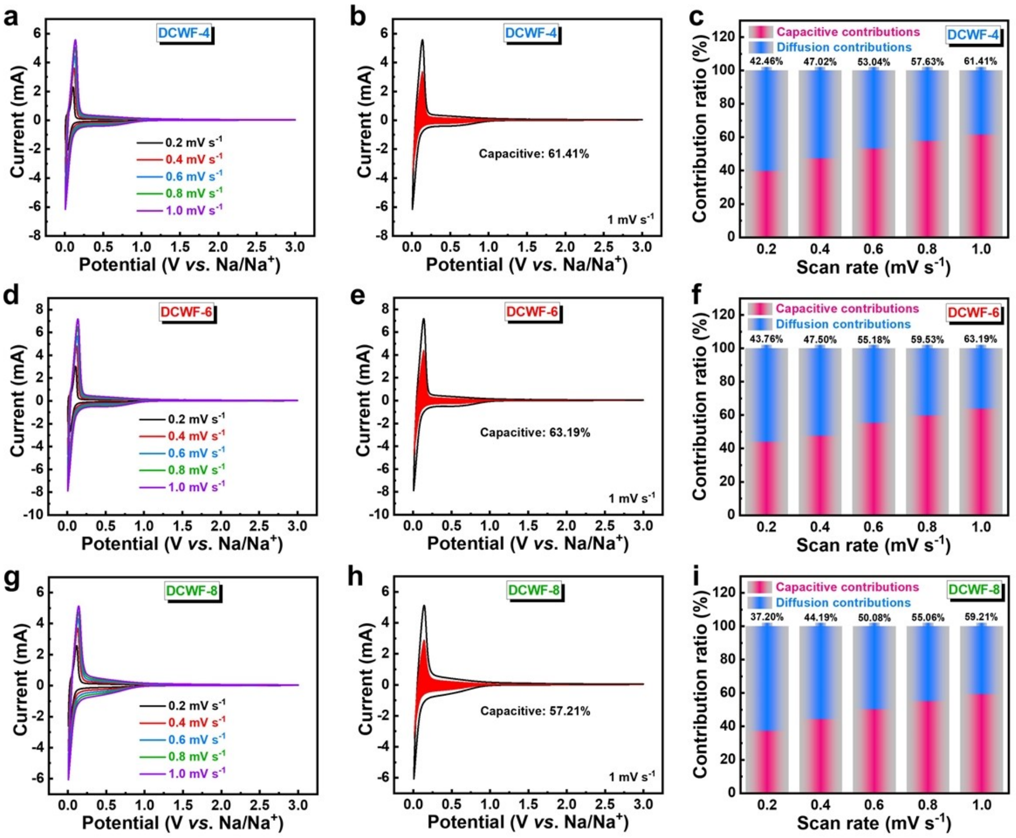

Fig. S13 Cyclic voltammetry curves of DCWF–4 (a), DCWF–6 (d) and DCWF–8 (g) electrodes with scan rates from 0.2 to 1.0 mV s^{-1}. The distribution of capacitive behaviors of DCWF–4 (b), DCWF–6 (e) and DCWF–8 (h) measured at 1 mV s^{-1}. The contribution ratio of the capacitive capacity of DCWF–4 (c), DCWF–6 (f) and DCWF–8 (i) electrodes at various scan rates.

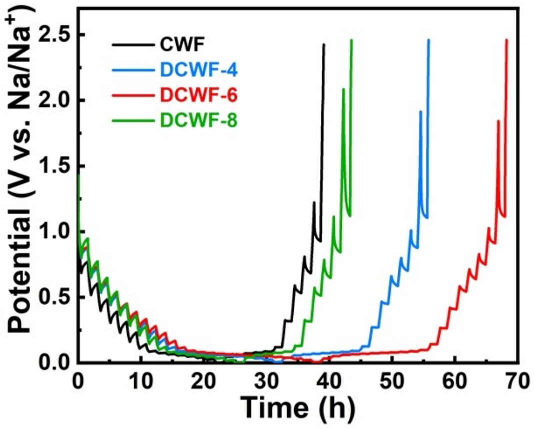

Fig. S14 GITT curves for the CWF and DCWF–*P* electrodes.

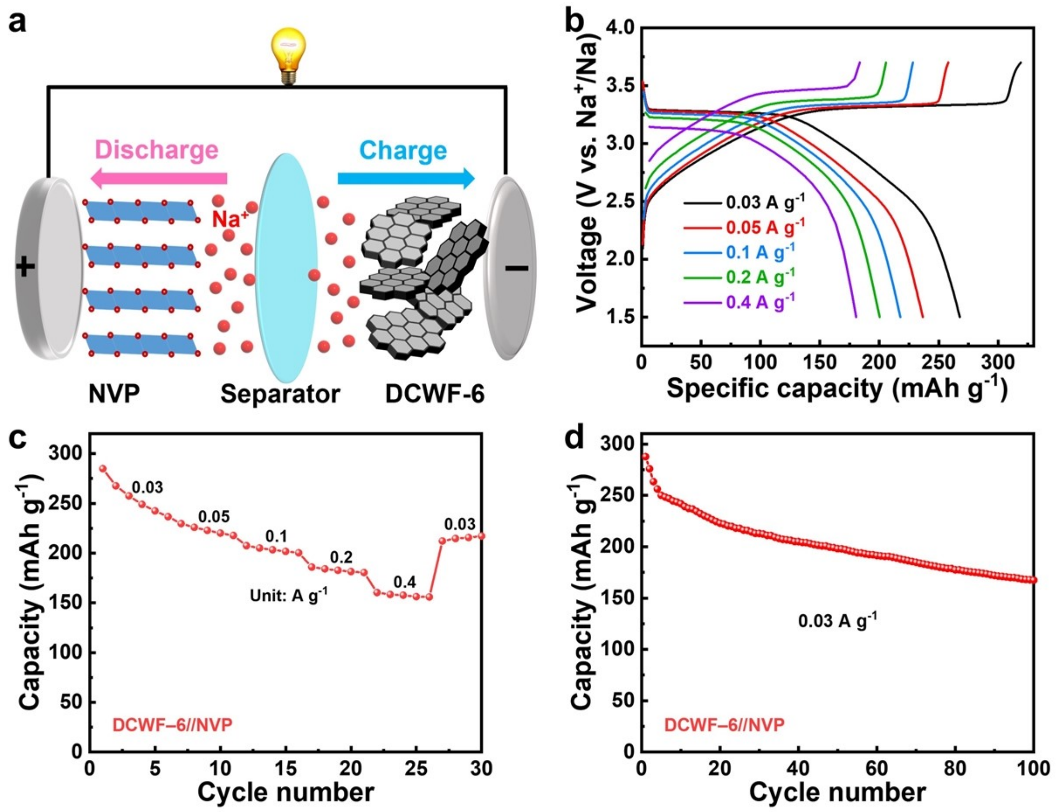

Fig. S15 Electrochemical performance of the full-cell using the DCWF–6 anode and the $Na_3V_2(PO_4)_3$ cathode. Schematic illustration of DCWF–6//NVP battery (a). Charge–discharge curves (b) of DCWF–6//NVP battery at various current densities. Rate performances (c) and cycling performances at the current density of 0.03 A g^{-1} (d).

Table S1 Percentages of various C configurations in CWF, DCWF–*P* and DCWF–*x*.

Samples	**C distributions/%**			
	sp^2	sp^3	**C–O**	**C=O**
CWF	51.75	19.35	17.55	11.35
DCWF–4	67.92	17.07	9.19	5.82
DCWF–6	68.86	13.67	9.18	8.25
DCWF–8	63.07	16.18	9.76	10.99
DCWF–20%	55.61	15.45	16.06	12.88
DCWF–80%	64.22	12.04	10.78	12.96